

Evaluation of Semi-Automatic Compositional and Microstructural Analysis of Energy Dispersive Spectroscopy (EDS) Maps via a Python-Based Image and Data Processing Framework for Fuel Cell Applications

To cite this article: Mariah Batool et al 2023 J. Electrochem. Soc. 170 054511

View the article online for updates and enhancements.

You may also like

- Development of a Hydrogen Contaminant Detector
 Charles Joseph Banas, Abdurrahman Yilmaz, Bryan Aponte et al.
- Differences in Metabolite-mediated Toxicity of Tamoxifen in Rodents vs. Humans Elucidated with DNA/microsome Electro-optical Arrays and Nanoreactors Linlin Zhao, Sadagopan Krishnan, Yun Zhang et al.
- Structure-property correlations and scaling in the magnetic and magnetocaloric properties of GdCrO₃ particles Jianhang Shi, Theodore Sauyet, Yanliu Dang et al.







Evaluation of Semi-Automatic Compositional and Microstructural Analysis of Energy Dispersive Spectroscopy (EDS) Maps via a Python-Based Image and Data Processing Framework for Fuel Cell Applications

Mariah Batool,^{1,2} Andres O. Godoy,^{2,3} Martin Birnbach,³ Dario R. Dekel,⁴ and Jasna Jankovic^{2,3,z}

Computer-aided data acquisition, analysis, and interpretation are rapidly gaining traction in numerous facets of research. One of the subsets of this field, image processing, is most often implemented for post-processing material microstructural characterization data to understand better and predict materials' features, properties, and behaviors at multiple scales. However, to tackle the ambiguity of multi-component materials analysis, spectral data can be used in combination with image processing. The current study introduces a novel Python-based image and data processing method for in-depth analysis of energy dispersive spectroscopy (EDS) elemental maps to analyze multi-component agglomerate size distribution, the average area of each component, and their overlap. The framework developed in this study is applied to examine the interaction of Cerium Oxide (CeO_x) and Palladium (Pd) particles in the membrane electrode assembly (MEA) of an Anion-Exchange Membrane Fuel Cell (AEMFC) and to investigate if this approach can be correlated to cell performance. The study also performs a sensitivity analysis of several parameters and their effect on the computed results. The developed framework is a promising method for semi-automatic data processing and can be further advanced towards a fully automatic analysis of similar data types in the field of clean energy materials and broader.

© 2023 The Electrochemical Society ("ECS"). Published on behalf of ECS by IOP Publishing Limited. [DOI: 10.1149/1945-7111/acd584]

Manuscript submitted August 9, 2022; revised manuscript received April 17, 2023. Published May 24, 2023.

Supplementary material for this article is available online

With the progression of materials from being discovered coincidentally to being designed and optimized strategically, there has been an imminent need to analyze and model materials for specific applications. This process can nowadays be facilitated by the power of advanced microscopy, and image and data processing. Digital image and data processing has found a plethora of applications in the field of materials science ranging from detailed morphological and structural analysis of materials to the study of their degradation and failure.^{2–7} Image processing is most widely implemented to extract valuable information from a more extensive set of materials characterization data and to understand and predict structureproperty correlations. However, to ensure the accuracy of results obtained from image processing, it is vital to have a systematic recognition of the features and the ability to process them swiftly for efficient analysis. Unfortunately, digital image processing comes with complications and challenges since microstructural images have a series of inherent issues, such as noise, low resolution, low illumination, inadequate color balance/contrast, and insufficient sharpness, among others. These issues can cause analysis to be complex for manual and automated techniques.^{8–11} Manual image processing is subjected to human error, experience, and bias due to varying opinions on what constitutes a particle, grain, grain boundary, defect, etc., within a microstructure. In addition, for the measurements to be statistically representative, they require repetition of both the data acquisition and processing, which becomes a burdensome and time-consuming task. Manual methods are, therefore, very slow and laborious. With automation, microstructural analysis, and measurements are conducted within seconds with improved consistency. However, microscopic images are often influenced by noise, which is the inclusion of random and false signals due to external conditions produced by contamination, sensors, detectors, and amplifiers. Such conditions can make features

like particles, grain boundaries, and materials interfaces challenging to perceive, or can create the appearance of features that are not real. ^{13,14} Therefore, one of the most difficult tasks of automated image processing is guaranteeing that the software is representing the material features accurately. The main image processing operation involves the digitization of the image, which can be graphically represented by Fig. 1. ^{15,16} However, although computer-based automated image processing has its challenges, it is far superior and has unarguably overshadowed manual image processing techniques in recent decades.

Such favorable characteristics of image processing led researchers to realize its potential for providing valuable microstructural information in the process of improving the performance and efficiency of clean energy systems. ^{17–19} Particularly, inspecting individual and collective characteristics of microstructural features of materials constituting a fuel cell such as electrodes, catalysts, and electrolyte membranes can help predict electrochemical behavior down to the nanoscale. 20-23 Besides composition, researchers validated the current density variations, ohmic and mass transport resistance, fuel transport mechanism, degradation, and structural stability. Hence, the overall fuel cell performance and durability are significantly influenced by a fuel cell's electrode microstructure and the distribution of each component in it.^{24–31} Therefore, to facilitate the development of efficient electrodes and fuel cells, and to establish statistically relevant correlations between the microstructure and performance, novel methods of automated image processing are required. In the area of fuel cells, image processing has been successfully utilized for distinguishing between different phases, porosity, and electrocatalyst particle size measurements, as well as for the study of the distribution of water within the catalyst layer. 32-41 However, typically, automated image processing for fuel cells involves using data extracted from transmission electron microscopy (TEM) or scanning electron microscopy (SEM) without taking into account elemental composition. 42,43 Furthermore, using

¹Institute of Materials Science, University of Connecticut, Storrs, Connecticut 06269-3136, United States of America ²Center for Clean Energy Engineering, Department of Materials Science and Engineering, University of Connecticut, Storrs, Connecticut 06269-5233, United States of America

³Department of Materials Science & Engineering, University of Connecticut, Storrs, United States 06269-3136, United States of America

⁴The Wolfson Department of Chemical Engineering, and The Nancy & Stephen Grand Technion Energy Program (GTEP); Technion—Israel Institute of Technology, Haifa 3200003, Israel

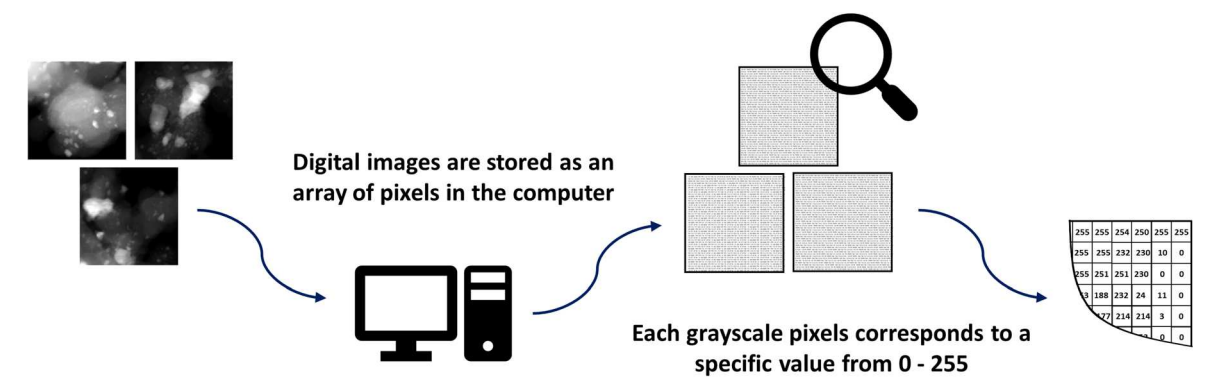


Figure 1. Image digitization process.

greyscale TEM and SEM images often makes it challenging to differentiate between various components in the material. To address this challenge, scanning transmission electron microscopy with energy dispersive spectroscopy (STEM-EDS) can be used to provide elemental maps with spatial component distribution, enabling this differentiation and offering a whole range of new possibilities for automated spectral data analysis.

Several spectral data processing approaches using EDS data, mainly in conjunction with SEM, have been developed and reported for a wide range of applications such as automatic particle size analysis of nano-materials, mineral constituents in rocks, inclusions in metals, contaminants in pharmaceutical products, air or water particulates, gun-shot residue in forensic science, pathological tissue in biomedical research, and automated identification of different phases and calculation of area, perimeter or compactness in a sample. 44-48 Combined with the machine and deep learning algorithms, SEM-EDS data have been used to investigate the morphology, size, and structure of particles or phases in a sample and to classify them. 49–52 However, given the complexity of some nanoscale multi-component systems such as catalyst-coated membrane (CCM) structures in fuel cells, the use of SEM-EDS is simply not viable due to spatial resolution and sensitivity limitations. In such cases, implementation of the STEM-EDS technique permits detailed analysis of individual regions within CCMs, demonstrating the interaction of different components such as catalyst particles, carbon support, and ionomers that may impact the fuel cell's performance. Some researchers have used image analysis on STEM-EDS data to study other complicated material systems, for example, to investigate channel thicknesses for flash memory devices, precipitates in Inconel 625 super alloy, and core and shell sizes for spherical semiconductor nanocrystal systems with minimum human intervention. 53–56 However, as far as we know, no such automated or semi-automated approach combining both spectral and image processing has been adopted and documented for fuel cell-related research yet, especially not when using high-resolution STEM-EDS. The development and application of an automated approach to analyze large sets of statistically relevant imaging and spectroscopy data would significantly reduce the analysis time and open new opportunities in the systematic study of structure-property correlations. Scenarios, where such an approach would have been beneficial include confirming the distribution and agglomeration of platinum (Pt) catalysts and ionomer in the fresh and degraded catalyst layers, distribution of Mg on carbon support for PtxMg/C-based catalyst layer in proton exchange membrane (PEM) fuel cells, quantification of corrosion by-products (i.e. Ni and Fe cations in the anode and membrane resulting from use of stainless steel liquid-gas diffusion layer in PEM electrolyzers), estimating the amount of Cr deposition in different types of lanthanum based-cathodes during polarization in solid oxide membrane fuel cells (SOFCs), to name a few.⁵

In this study, we report an in-house developed semi-automatic Python-based code able to process a set of spectral data within minutes, applied to a study of anion-exchange membrane fuel cells (AEMFCs). Although we focus our study on AEMFCs, we believe that with further optimization, our code can be successfully employed in different studies pertaining to other electrochemical systems as enumerated above, and broader. AEMFCs are fuel cells that conduct anions through solid polyelectrolyte anion-exchange membranes and operate under moderate temperatures (0 °C—120 ^oC) with a variety of fuels. ^{64–67} AEMFCs can utilize Palladium (Pd)based catalysts, 68,69 which are significantly more abundant alternatives to the scarce Pt catalysts typically used in proton-exchange membrane fuel cells (PEMFCs). Pd-based catalysts suffer from sluggish hydrogen oxidation reaction (HOR) kinetics, which could be potentially avoided by combining Pd nanoparticles with Cerium Oxide (CeO_x) through controlled surface reactions and ensuring sufficient Pd-CeO $_x$ interaction for a prospective increase in the catalytic activity. The increase in catalytic activity is ascribed to the flow of OH⁻ ions from CeO_x to Pd, which not only significantly improves the rate of the Volmer reaction but also undermines the hydrogen binding energy in the Pd-H bond.⁷⁴ Therefore, the close and more intimate interface between Pd and CeO_x is expected to improve the performance of these catalysts. However, this hypothesis, as well as the effect of other parameters, such as Pd and Ce particle/agglomerate size distribution, in addition to the contact area between them, needs to be further studied. A thorough investigation can be carried out by microscopy and spectroscopy. To support this analysis, we developed a Python-based data and image processing framework that uses STEM-EDS elemental maps and spectral data of Pd-CeO_x catalysts to produce visual and numerical results and correlate them to the electrochemical performance and durability of the AEMFCs. The exclusive utilization of such processing techniques on STEM-EDS data for the evaluation of fuel cell electrodes is being reported for the first time in this study. The study also reports the sensitivity analysis, discusses the effect of various input parameters on the calculated results, and compares them to a previously reported image processing technique used by Singh et al. 75

Methodology

The script for the image and data processing framework developed in this study was written in Python (version 3.9.2). The code uses different statistical functions, image and data processing, and plotting modules from several open-source Python libraries, i.e., NumPy 1.20.1, Pillow 8.3.2, Pandas 1.3.4, OpenCV 4.5.4, SciPy 1.6.1, Scikit-Image 0.19.1, and Matplotlib 3.3.4. The graphical user interface (GUI) was developed using the PyQT5 toolkit. This inhouse developed Python-based code was initially conceptualized at the Automotive Fuel Cell Cooperation, and further modified, refined, and implemented in this study. The idea in this particular study (but applicable to other multi-component systems), was built around the fact that materials characterization data about Pd-CeO_x-based catalysts (although it can be a source of a vast amount of information) require a rigorous analysis procedure to get

"concealed" or underlying information not visible to the naked eye, such as percentage of the area where Pd and CeO_x overlap (contact area, which is expected to benefit the HOR activity) and the catalyst particle or agglomerate size. Thus, three different catalyst samples supported by carbon (C), i.e., n CeO_x -Pd/C with varying compositions (where n denotes the bulk atomic ratio of Ce/Pd): 0.24 CeO_x -Pd/C, 0.38 CeO_x -Pd/C, and 0.59 CeO_x -Pd/C labeled as DD08, DD09, and DD16, respectively, were taken into consideration. A detailed description of the samples, their fabrication, and testing are discussed in our previous study and a thorough comparison of the adopted approach to the image processing by ImageJ used by Singh et al. is hereafter also presented. The Agraphical overview of the whole data processing process in our study is shown in Fig. 2 and discussed below.

Acquisition and processing of raw data.—Thermo Fisher Talos F200 TEM operated at 200 kV in the high-angle annular dark-field (HAADF) STEM mode with an in-built ChemiSTEM-based EDS system was used to acquire high-resolution images and corresponding elemental maps of 768×768 pixels for all catalyst samples under consideration. All images were obtained at a constant magnification of $910,000\times$ and their elemental maps were visualized in hyperspectral mapping mode with Bruker Esprit Microanalysis software (v 1.9). The feature of hyperspectral mapping in Esprit is termed HyperMap and allows the acquisition and storage of spectrum data for each pixel of the image and can be established as the major data source for the program developed in this study. The types of raw elemental maps that were obtained initially are shown in Fig. 3.

The raw maps were then pre-processed using the Esprit software with the Cliff-Lorimer quantification method to remove background and deconvolute the spectral peaks (to form, so-called, QMaps). The Cliff-Lorimer method is based on the following formula:

$$\frac{I_A}{I_B} = k_{AB}^{-1} \left(\frac{n_A}{n_B} \right)$$

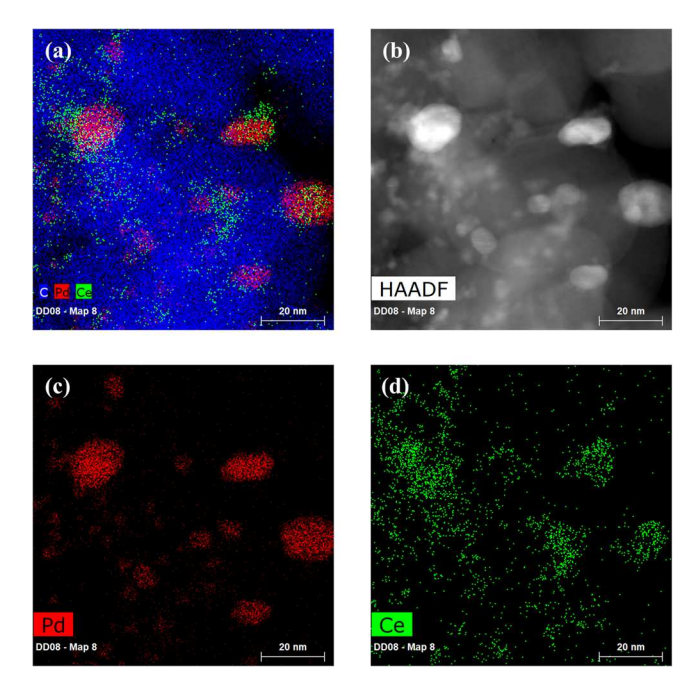


Figure 3. (a) Raw STEM/EDS elemental map of C, Ce, and Pd (b) HAADF image (c) Raw Ce elemental map (d) Raw Pd elemental map (Scale bar = 20 nm).

where A and B refer to any two elements, k_{AB} is the Cliff-Lorimer sensitivity factor between them, I_A and I_B are the integrated EDS peak intensities, and n_A and n_B are the atomic density percentages for the elements A and B, respectively. In general, the formula computes concentration ratios by relating the measured signal intensities to the calculated intensities of pure elements. This method is typically applied to EDS quantification in STEM (not in SEM) due to the low sample thickness used, which allows the involved absorption and fluorescence correction to be neglected. The resulting individual elemental QMaps of EDS X-ray net intensities

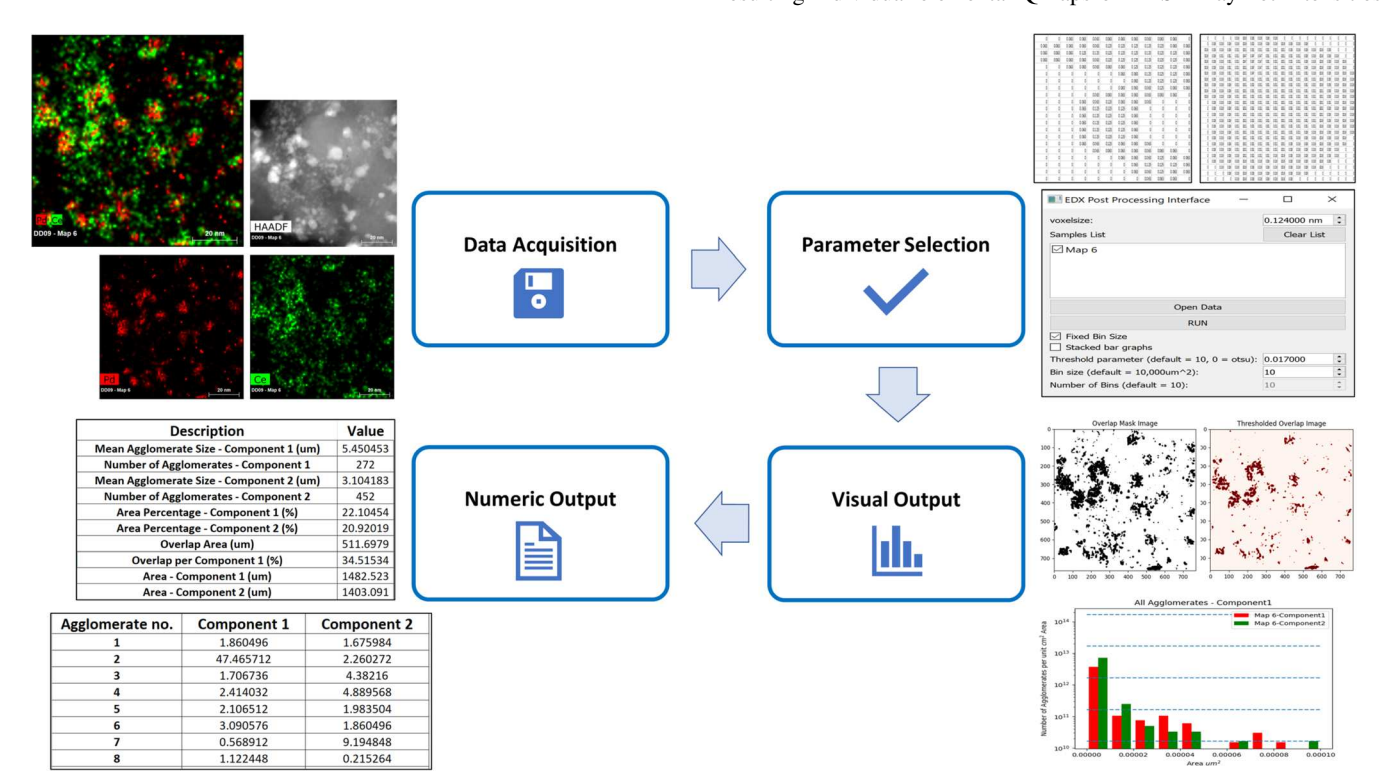


Figure 2. Visual overview of the developed image and data processing framework.

of Ce and Pd were subsequently saved as text files in ASCII format. ASCII format is the standard code used for information exchange and is typically used in data processing. In ASCII format, each character is stored in 8 bits of memory and allocated a number between 0 and 255. 81,82 The software thus allocates a specific numeric value in the text file according to the X-ray net intensity data for each pixel of the QMap. This text file is a complete roadmap of the intensity of each X-ray net count signal and its precise location in the respective elemental map. Pre-processing of the elemental maps can be performed using different binning (resolutions): e.g., with the resolution 1, each pixel is separately processed, and its processed value is assigned to the same pixel; with the resolution 0.5 (1/2), four pixels are averaged (the signal is combined, processed and the final values equally divided between the four pixels); with the resolution 0.125 (1/8), sixteen pixels are averaged (For more detail, see Fig. S1). Consequently, resulting net count values of the same pixel (e.g., ascribed to a particle) in text files of the same OMap at different resolutions are different. An example of different net count values at different QMap resolutions is shown in Fig. 4. Apart from choosing the QMap resolution, Esprit also allows users to choose between different types of map and image filters. Map filters are applied directly on the net count signals contained in the map while image filters are applied only to the overlay image to enhance the visibility of features (For more detail, see Figs. S2 and S3). The effect of the QMap resolution and filters on the results obtained is detailed in Supplementary Material. The names of text files for Pd were labeled as "component1.txt" and all the text files for Ce were labeled as "component2.txt" and saved in separate folders with each sample's name and map number. Furthermore, the STEM image for each raw map taken with HAADF imaging was saved in the same folder in TIFF format and labeled as Mask. The specified labeling was carried out to be traceable by the code for processing as well as to be able to be used with any two components at any time.

Adjustment of input parameters and sensitivity analysis.—To start the data processing in the Python framework, the methodology given in Fig. 5 was adopted (as described in more detail in the Supplementary Material). The pixel size needs to be adjusted according to the pixel size of the raw map, while an appropriate threshold value needs to be selected to ensure that the code considers only the specified component's true signal and disregards any noise the map might contain. Appropriate bin size or the number of bins needs to be selected for an apt statistical representation of area (agglomerate, particle, etc.) size distribution histograms.

It is crucial to emphasize here that for an appropriate adjustment of input parameters in the program interface, an optimal preadjustment of parameters associated with pre-processing software, Esprit is vital. To ensure the extraction of valid, statistically representative, and consistent results with the developed code, a thorough sensitivity analysis was performed here to investigate the effect of changes in each parameter on the output generated by the program, while keeping all other parameters constant. This local sensitivity analysis for individual parameters helped gain insight into the type of impact they create on the program output. The impact of each parameter was assessed and compared against other parameters and subsequently categorized as a no/low, moderate, or high impact parameter. The list of input parameters, along with a detailed discussion and a qualitative assessment of their impact on the output results influence on results, is presented in the Supplementary Material section.

Execution of post-processing analysis.—Once the parameters are set and the EDS Post-Processing Program is allowed to run, the code runs through the text files and scans all the numeric values listed in the text file of each component, and applies the userthresholding algorithm. This step is accomplished using data browsing, sorting, and processing in the NumPy library. The program also collects and lists all the available threshold values from the individual maps of each component being processed, allowing users to make informed decisions regarding the best selection of the user-defined threshold value. After the user-defined thresholding of individual map files, statistical and mathematical operations are applied to the data to determine the desired parameters. For example, Pd and Ce overlap is calculated using a mathematical comparison of signals in each pixel (e.g. if a pixel contains Pd X-ray net counts in the Pd text file and Ce X-ray net counts in the Ce text file, an overlap is identified). The agglomerate or overlap areas were simply calculated by multiplying the number of pixels containing the desired signal (e.g., Pd, Ce, or Pd/Ce overlap) by the resolution of the pixel. Mathematical computation of the respective individual and overlap areas and percentages are then carried out using NumPy data processing. The processed data is then segmented, rearranged, and saved in TIFF format using the Pillow library. This generates the resulting individual masks and thresholded images for each map and their combined overlap mask and thresholded image. The mask refers to a binary image that has assigned zero (black color) to all pixels above a specified threshold value and 255 (white color) to all pixels below the specified threshold value. Mask images of individual maps are thereby

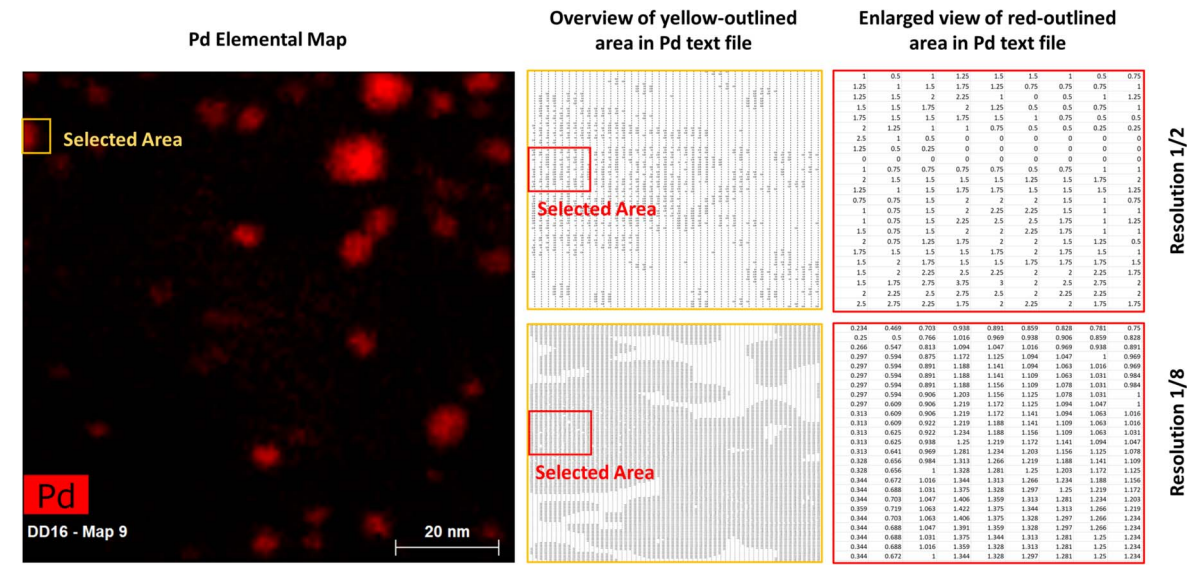


Figure 4. Overview of the corresponding ASCII text files to specific elemental map resolutions.

Process Flowchart

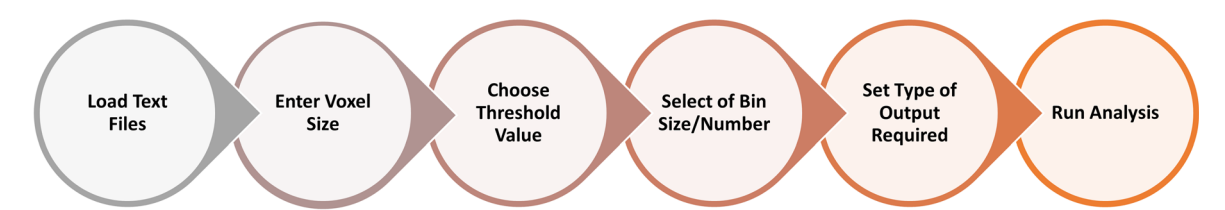


Figure 5. Process flowchart for running analysis in the program interface.

generated by simply assigning zero (black color) to all original X-ray net count signals in a map irrespective of the chosen threshold value, while the thresholded images of individual maps are generated by selectively removing potential noise signals from the original X-ray net counts by considering and only visualizing signals equal to and above the chosen user-defined threshold value. For the Pd-Ce overlap area determination, the overlap data is already sorted using the mask and thresholded map values, so any additional binarization is not required for the construction of the overlapping mask and its corresponding thresholded image. The plotting and visualization of these images are carried out using the Matplotlib module. The collection of these images constitutes a major part of the visual output given by the developed code. This visual data is further processed via image processing modules to generate further results, as discussed below. OpenCV is utilized to load and read data from all images, while Scikit-Image and Scipy are collectively used for labeling, segmentation, and computation of each particle/agglomerate size in the individual as well as overlap maps. The program also creates histograms for the agglomerate size distribution of each component individually and collectively. All numerical results of the program, including calculation of individual map areas and overlap areas along with their corresponding percentages with or without the user-defined threshold value, number, and size of agglomerates and mean agglomerate sizes are automatically saved in an Excel file using Pandas. By default, all the measurements are carried out in micrometers (μ m).

Results and Discussion

As mentioned above, the data and image processing method introduced in this study generates two different forms of outputs: graphical and numerical. The different results that were obtained for each concentration of the catalyst samples under observation are therefore presented using these outputs. It can be aptly implied that the variety of outputs generated by the developed program in the form of masks, thresholded images, overlap images, agglomerate size distribution charts, component area overlap, and calculation data sheets offer a wide range of result datasets that can be crucial for a comprehensive study of any sample under consideration.

For reliable use of the discussed semi-automatic EDS analysis interface, sensitivity analysis results were used as the base for the selection of optimal input parameters. As mentioned above, these parameters are associated with EDS pre-processing software, Esprit, and the developed post-processing framework. A detailed argument about the type of influence each of the input parameters depicts upon the computed results, along with the justification for the selection of a chosen value of each to run the main analysis, is provided in the Supplementary Material. Moreover, for an accurate substantiation of the developed data and image processing framework, a thorough comparison with a conventional analysis technique (i.e., ImageJ used by Singh et al. for calculation of interfacial contact area) is presented.⁷⁵

Sensitivity analysis.—The parameter sensitivity analysis showed a different relative effect on the code output results (quantified through Pd and Ce area comparison), as shown in Fig. 6. The impact

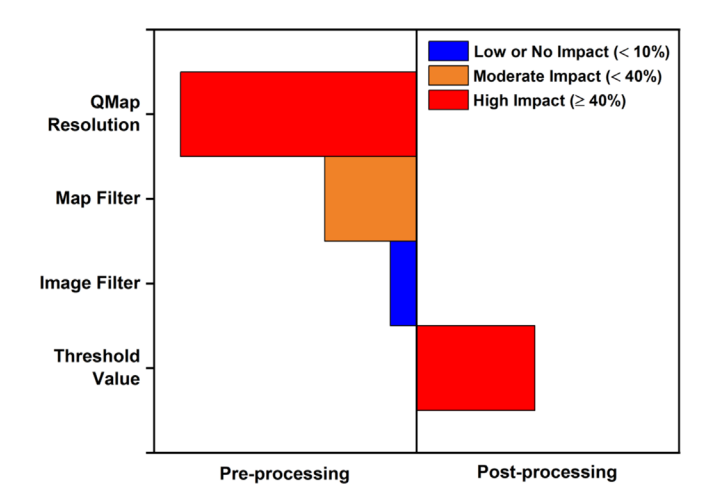


Figure 6. Sensitivity analysis of all input parameters of the study.

for each parameter is quantified by the percentage difference between the lowest and the highest value of Pd and Ce area calculations with respect to variations in a specific parameter while keeping all other parameters constant. The strongest effects are caused by the QMap resolution and EDS signal thresholding; users need to make a careful choice to perform an accurate analysis. After investigating the potential effects of different parameters upon output results generated by the developed code as part of the sensitivity analysis a set of ideal parameters were chosen (Table I). For more information, see Supplementary Material.

Sample analysis and correlations to performance.—Interfacial contact area calculation.—Using the set of parameters in Table I, the code analysis for all ten maps of the three catalyst samples in consideration was carried out, compiled, and represented. In addition, for comparison purposes, non-thresholded EDS maps were also used.

The complete analysis of all the samples returns a large visual and quantitative dataset which enables the investigation of how different Pd and Ce loadings in different catalyst samples affect Pd and Ce agglomerate size and distribution, as well as the Pd-Ce interfacial contact area/percentage. In terms of graphical output, Fig. 7 shows an example of a few elemental maps and their output before and after thresholding (showing large variation) generated by the developed code.

It should be noted that the dataset is exposed to the minimum level of user-defined thresholding as the value of 0.016 is the lowest possible net intensity value observed at the given map resolution and, therefore, the threshold value of 0.017 selectively eliminates minimum level background signals or noise (having net count value of 0.016) from the thresholded image. It also ensures that the presence of any actual X-ray net count signal is not missed while computing the results.

The quantitative output of the average interfacial contact area between Pd and Ce as well as the average percentage of Pd covered

Table I. List of selected parameters for running the main analysis.

List of parameters	Selected option/values
Map Resolution	1/8
Map Filter	Automatic
Image Filter	None
Voxel Size	0.124 nm
Threshold Values	T = 0 (No Thresholding) & $T = 0.017$ (With Thresholding)

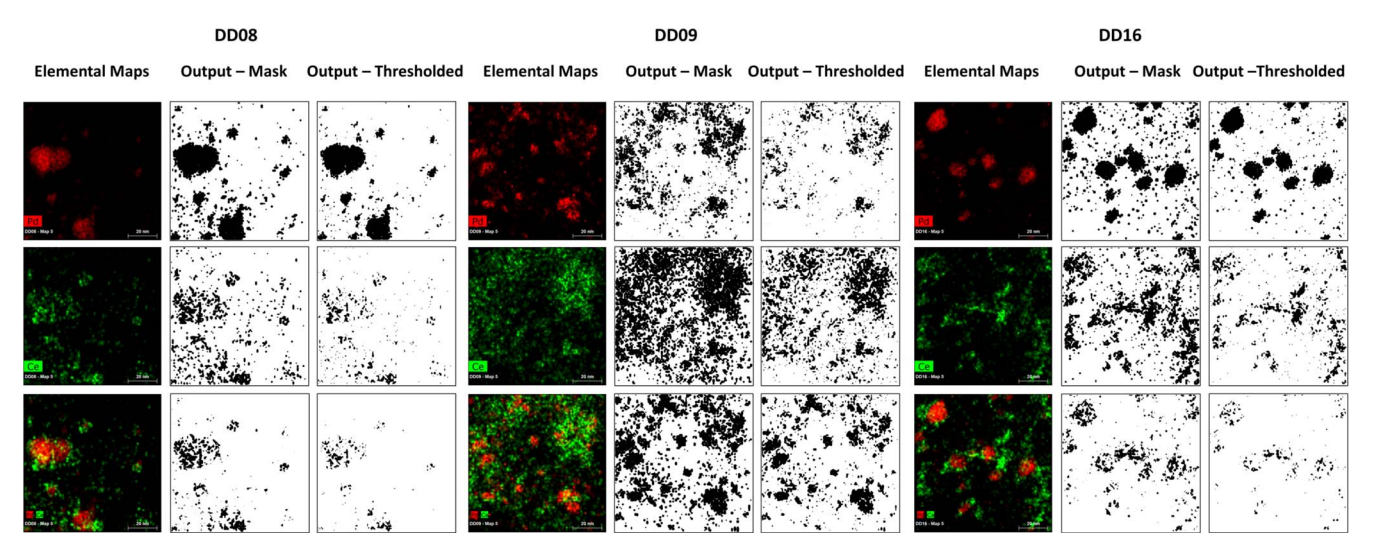


Figure 7. An example of input pre-processed elemental maps, their corresponding masks, and output results after thresholding for Pd (1st row), Ce (2nd row), and Pd-Ce overlap data sets (3rd row) for three different catalysts, as generated by the code (Scale bar = 20 nm).

by Ce for all samples along with standard error (SE) were compiled and illustrated in graphical form in Fig. 8. The average interfacial contact area and the average percentage of Pd covered by Ce for each catalyst sample were computed by averaging the values of interfacial contact areas and individual percentages of Pd covered by Ce for all ten maps of each sample, respectively. The comparison with the manual processing using ImageJ is added as well to illustrate the possible variation in the analysis, of which a user needs to be aware. 75

It can be noted from Fig. 8a that the average overlap area calculations for ImageJ and the developed code not only vary to a great extent quantitatively but also do not follow the same trends.

While the reported ImageJ results show an increase in the average interfacial area from sample DD08 to DD09, they also show a decrease in the same from sample DD09 to DD16 (although within the standard error). However, the code output shows a progressive increase in the average interfacial area from DD08 to DD16. It is worth noticing that the increase in the average Pd-Ce interfacial area determined by ImageJ in the reported study is very significant (\sim 40%) from sample DD08 to DD09, yet the same decreases by a small percentage (\sim 3.6%) from DD09 to DD16 (even though the actual atomic Ce/Pd ratio increases 58% from sample DD08 to DD09, and further by 55% from DD09 to DD16. The reported study explains this difference in the trends by the deposition of CeO_x onto

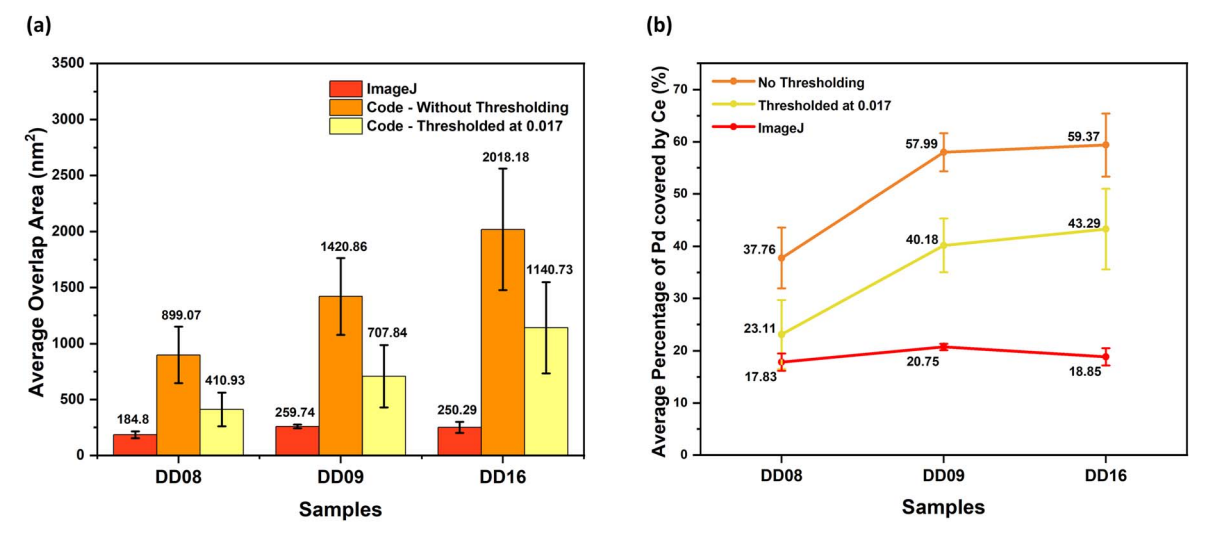


Figure 8. (a) The average interfacial overlap area between Pd and Ce as calculated by ImageJ and the code for each catalyst powder with standard error (b) The average percentage of Pd covered by Ce (overlap) calculated by ImageJ and the code for the same maps for each of the catalyst powders with standard error.

carbon rather than Pd in sample DD16 and the formation of large ${\rm CeO_x}$ agglomerates. When processed by the developed code, the increase in the Ce/Pd overlap very well agrees with the actual increase in Ce/Pd atomic ratio, resulting in a 58% increase from sample DD08 to DD09, and an additional 42% from DD09 to DD16 for non-thresholded processing, and 72% and additional 62% increase, respectively, for the thresholded processing. This difference between ImageJ and the developed code results can be explained by their fundamentally distinct approaches. For the calculation of the interfacial contact area of Pd and Ce, ImageJ follows an entire image processing-based methodology, relying on user judgment, while the introduced code framework is largely based on spectral data analysis, with minimal user influence.

The representation based on the average percentage of Pd area covered by Ce rather than the absolute Ce/Pd contact area (in nm²) was investigated as well, as shown in Fig. 8b. It was noticed that even though the overall trends do not differ even in terms of overlap percentage, the overall meaning can convey a much clear picture when quantified in terms of the percentage of total interfacial contact area over total Pd area. The trends show that as per the code's output, there is an approximately 54% increase without thresholding and a 74% increase with thresholding in the interfacial area percentage from sample DD08 to DD09. This trend agrees well with the actual increase in the Ce/Pd atomic ratio of 58%. However, the ImageJ results show an increase of \sim 16% only. The interfacial area percentage between samples DD09 to DD16 shows an increase of 2.4% for the code without thresholding and 7.7% for the code with thresholding, pointing to a large amount of CeO_x not being in contact with Pd (since the actual atomic Ce/Pd ratio increases by 55% from DD09 to DD16). The ImageJ trend shows a decrease of 9.2% in interfacial area percentage between the same samples. Therefore, the remaining analysis was continued using the code only, and not ImageJ analysis. Furthermore, our conclusions were further drawn from the thresholded maps, as proven to result in the most realistic representation of the actual samples. Non-thresholded code results were only added for the comparison and the reader's judgment of the accuracy of the results.

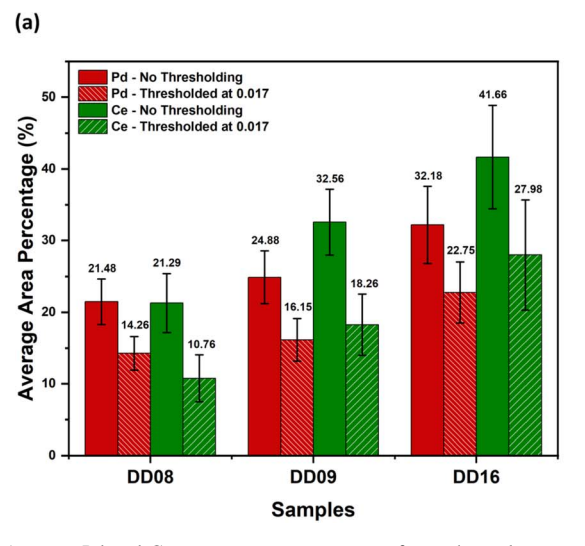
To elucidate the observed trends further, the current study also calculated the average percentages of Pd and Ce area covering the map area for all catalyst samples under consideration, and the calculations are plotted in Fig. 9. The average percentages of Pd or Ce refer to the average value of the percentages of Pd or Ce areas divided by the total map area for all ten maps of each sample. These Pd and Ce map area percentages would simulate the total amount of Pd and Ce per area (areal density).

Figure 9 shows a gradual increase in the average area percentage of Ce and Pd per map area from sample DD08 to DD16. A question arises why we would see such a trend, especially for the Pd area, since the overall amounts of the analyzed samples should be comparable (due to the same sample preparation method) (Ce area is expected to increase due to an increasing Ce/Pd atomic ratio in the actual sample). One plausible explanation would be that the dispersion (or agglomeration) of the samples is not the same, resulting in better dispersion and smaller agglomerates for DD08 than for DD09 and DD16, captured by each map. Indeed, our agglomerate size analysis in the next sections does confirm this explanation. Taking EDS maps at a lower magnification would normalize this Pd area trend.

When further analyzing the trends in Fig. 9b, an intersection point between Pd and Ce can be seen for the thresholded code results. This intercept represents a point at which average area percentages of both Pd and Ce are the same. In other words, at this point, there is the same areal density (amount) of Ce in a sample as Pd. It is fairly evident that the intersection point implying the Pd and Ce percentage for optimal interfacial contact area for maps without thresholding lies very close to DD08. Conversely, for the maps thresholded at 0.017, this point lies between DD08 and DD09. However, for both cases, the Ce area is much higher than the Pd area for DD16. Therefore, it may be deduced that the catalyst sample DD16 has an excessive addition of Ce. This may, in turn, affect the properties of the Pd-Ce catalyst. 83 This effect can be visually explained by Fig. 10, which shows the different stages of interfacial contact between Pd and Ce.83 Ideally, we are looking for optimal interfacial contact between Pd and Ce, as shown in Fig. 10b, without reaching a point where Ce is either too low (as in Fig. 10a) or too high (as in Fig. 10c).

By comparing Figs. 8, 9, and 10, it can be concluded that this excessive addition of Ce beyond the intersection point is rather unconscionable, unnecessary and, has little or no effect on an increase in interfacial contact area beyond a maximum coverage point. Moreover, the performance data for these three catalysts show the highest performance for the DD09 sample, whose Pd and Ce areas are closest to the optimal intercept point in Fig. 9.75

Agglomerate/particle size distribution.—In addition to the interfacial contact area and area percentage calculations, the developed code possesses the ability to compute agglomerate or particle size distributions for each map of all three catalyst samples (Without distinction between particles and agglomerates, we will use the term "agglomerate" for all features). This information is vital to understanding the behavior of the Pd and Ce particles and how they may



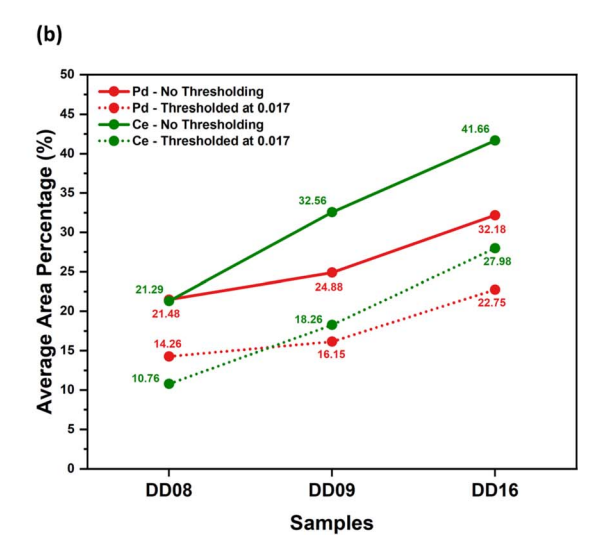


Figure 9. Average Pd and Ce area percentage per map for each catalyst sample computed by the developed code (a) Represented as a bar chart with standard error (b) Represented as trend lines.

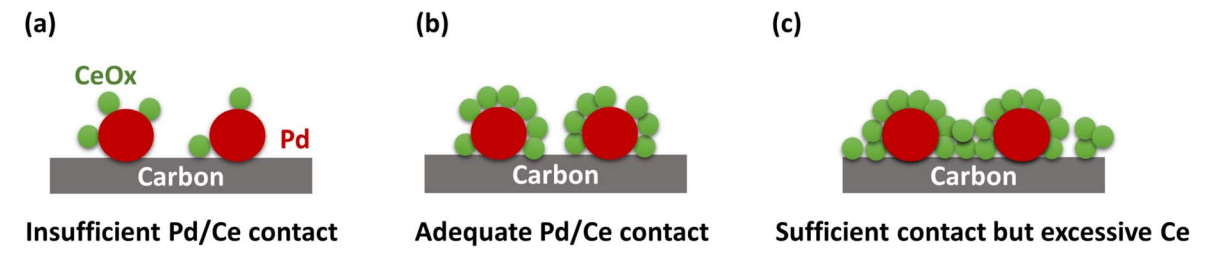


Figure 10. Different stages of interfacial contact between the Pd and Ce (a) Insufficient Pd-Ce contact (b) Adequate Pd-Ce contact (c) Sufficient Pd-Ce contact but with excessive Ce agglomeration.

affect the performance of the catalyst samples in the fuel cell. Figure 11 shows the combined logarithmic histogram for each agglomerate of Pd and Ce in each of the catalyst samples with and without thresholding. The logarithmic scale is chosen in this case to observe the agglomerate size distribution trend for a larger variation-based dataset of computed agglomerate sizes. All agglomerates less than 1 nm² have been neglected.

It can be seen from Figs. 11a and 11b, that in both cases, Pd and Ce histograms are positively skewed with a tail towards the right end. All histograms show an asymmetric distribution of agglomerate sizes, with most sizes ranging less than 10 nm². In Fig. 11b, Pd agglomerates tend to show a more homogenized size distribution in comparison with Ce agglomerates. Moreover, Pd agglomerates generally tend to decrease in size from sample DD08 to DD16, while the Ce agglomerates on the other end show a gradual increase in size distribution tail towards the right, implying the increased presence of relatively bigger agglomerates in sample DD16 in comparison with samples DD08 and DD09.

By comparing Figs. 11a and 11b, it can also be observed that there seems to be a large degree of variation between agglomerate sizes for Ce compared to Pd for results computed without thresholding. However, Pd and Ce both show a much more homogeneous

agglomerate size distribution for results subjected to user thresholding, with homogeneity increasing progressively from sample DD08 to DD16. This trend of increase in homogeneity is also much more perceptible in Ce than in Pd agglomerate size distribution. To get an improved interpretation of agglomerate size distributions, the average agglomerate size of Pd and Ce for each catalyst sample was also computed with and without thresholding and plotted in Fig. 12a.

From Fig. 12a, it is evident that the average agglomerate sizes for Pd and Ce tend to increase progressively from sample DD08 to DD16 with or without thresholding. However, the effect of the increase in average agglomerate size appears more pronounced for Ce in comparison to Pd. Sample DD08 tends to have, on average, slightly larger Pd agglomerates than Ce with and without thresholding, but eventually, in sample DD16, the average agglomerate size for Ce is greater than that for Pd. Also, the difference in average agglomerate size between Pd and Ce is much less in sample DD08, while the variation is largest in sample DD16. This behavior, in fact, supports our assertion of excessive Ce content in sample DD16 resulting in increased agglomeration. Furthermore, examining the lower and higher limits for standard error (SE) for each catalyst sample indicates that sample DD16 contains a lesser number of agglomerates compared to samples DD08 and DD09. This

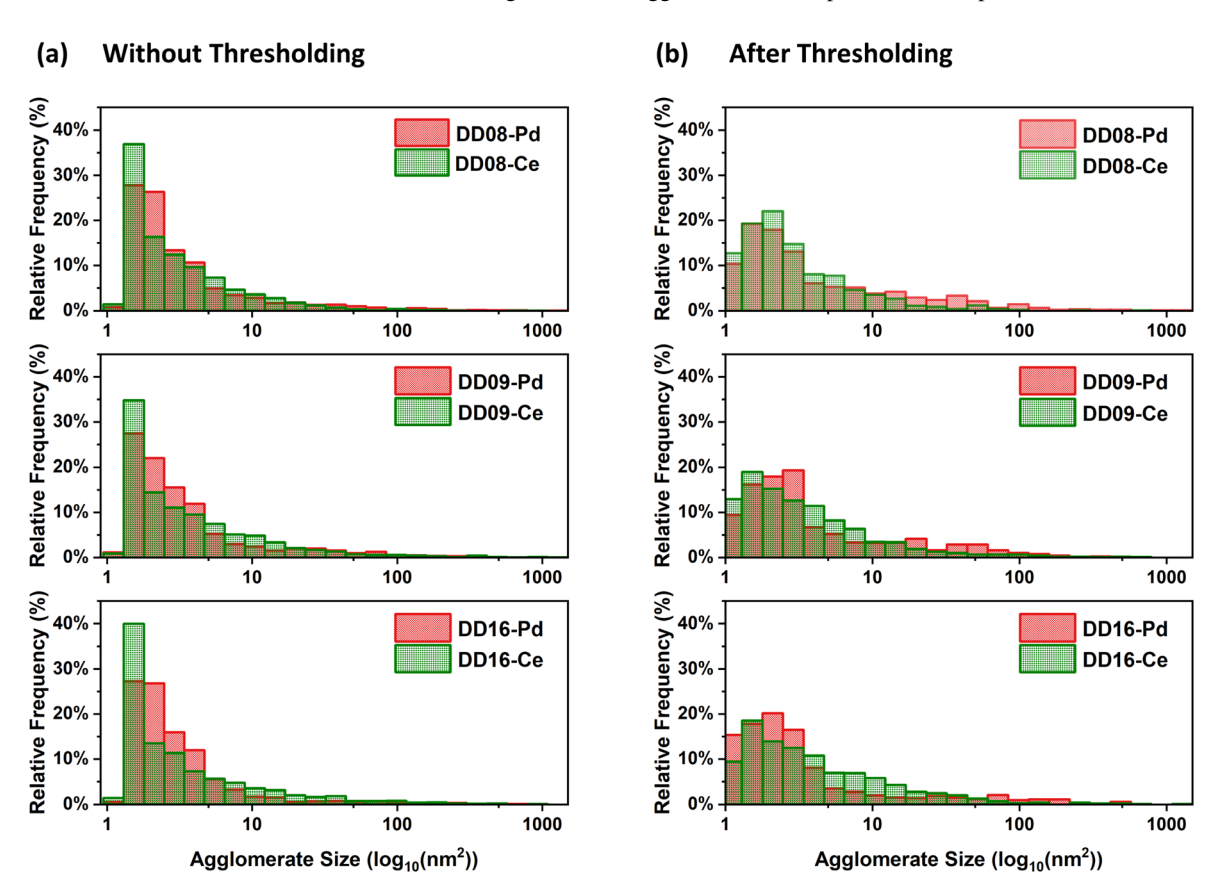


Figure 11. Histograms for Pd (red) and Ce (green) agglomerate size distribution within each catalyst sample (a) without thresholding (b) with thresholding.

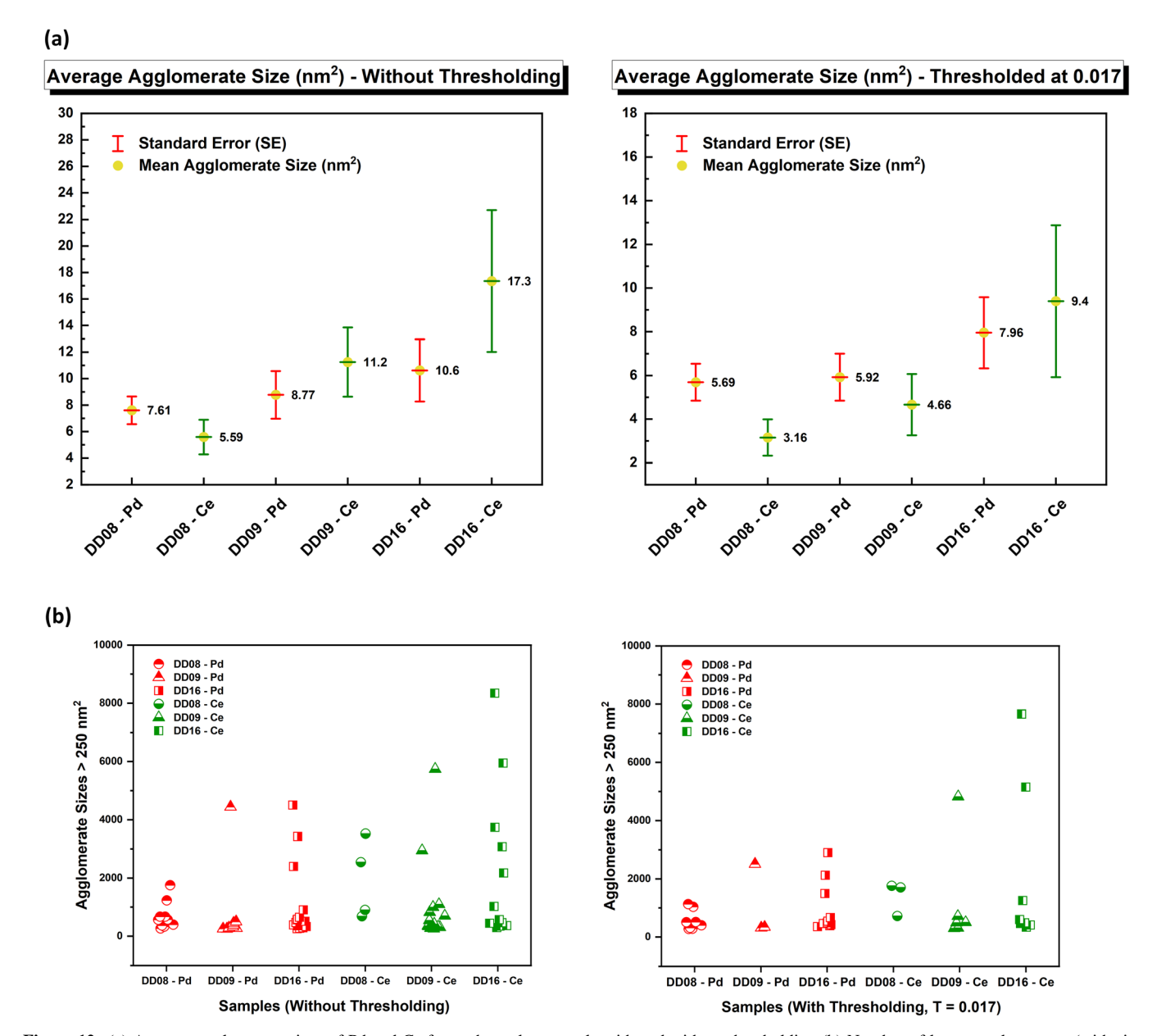


Figure 12. (a) Average agglomerate sizes of Pd and Ce for each catalyst sample with and without thresholding (b) Number of larger agglomerates (with sizes greater than 250 nm²) for each catalyst sample with and without thresholding.

information reflects that the estimation of mean agglomerate size is much more accurate and reliable in DD08 and DD09 in comparison with DD16. To elucidate the trend more clearly, agglomerate sizes greater than 250 nm² were plotted separately for each catalyst sample with and without thresholding in Fig. 12b.

In Fig. 12b, the number of larger agglomerates increases from sample DD08 to DD16 for both Pd and Ce. However, there are only a few agglomerates of Ce and Pd having sizes greater than 250 nm² and at most represent less than 1.3% of the total number of agglomerates in their respective samples. This result further supports the presence of the unnecessary amount of Ce in DD16, leading to a higher degree of agglomeration suitably substantiated by a higher number of larger agglomerates and larger average agglomerate size in results generated by the code. This theory can be experimentally verified by the low dispersity of CeO_x nanoparticles and their increased susceptibility to agglomeration, especially when present in excessive amounts. ^{84,85}

Furthermore, increased agglomeration of catalyst nanoparticles is linked by various researchers to the decline in overall fuel cell performance by decreased catalyst utilization, increased mass transport loss, and reduced conductivity. 86-88 Thus, it can be determined from the results of agglomerate size distribution that despite demonstrating the highest interfacial contact area between Pd and Ce, the effect of increased agglomeration might be the governing factor in reduced electrochemical performance in sample DD16 in comparison with sample DD09 as established through experimental data by Singh. 75 This finding also validates the fact that the optimum bulk atomic ratio of Ce/Pd does indeed lie between 0.24 and 0.59. Moreover, since code-generated results with userdefined thresholding have shown promising findings, it is appropriate to estimate that the optimum bulk atomic ratio lies closer to 0.38 (sample DD09) as justified by the intersection point of average Pd and Ce area percentages in Fig. 9. Nevertheless, it may also suggest that a bulk atomic ratio higher than 0.24 and slightly lesser than 0.38 may be able to reveal superior electrochemical performance than the one recorded.

In summation, it is befitting to note that the developed code with the right use of user-threshold value can help uncover a lot of information regarding the potential performance of catalysts used in AEMFCs. Additionally, most studies involving data processing have computed and reported results based on imaging data alone. ^{89–94} On the contrary, extraction of microstructural information from STEM in combination with elemental map data from EDS gives this method its distinctiveness in addition to the automatic computation of agglomerate size distribution and overlap area of the particles (which has not been reported before).

Conclusions

The data and image processing framework introduced in this study is a unique, automated, and promising method for the semi-automatic post-processing of STEM-EDS data, with an example application to catalyst analysis in AEMFCs. The code runs the pixel-by-pixel numerical analysis, keeping into account distinct agglomerates within the elemental maps, which might be overlooked during manual analysis; thus, it can effectively resolve problems associated with an extensive and exhaustive analysis of larger data sets. However, it can be concluded that the calculations also depend heavily upon the EDS map pre-processing software used to extract data for the code.

The study also points out that the selection of an appropriate threshold value is vital to ensure good precision of results generated by the program. The comparison of the data generated by the developed code to that reported by a previous study completed by the image analysis proved tremendously beneficial in establishing relevancy between excessive agglomeration, interfacial contact area calculations of Pd/Ce, and the different bulk atomic ratios of Ce/Pd in catalysts while potentially predicting the governing factor influencing the electrochemical performance of AEMFCs. The study prompted the investigation and collection of additional data about Pd and Ce microstructural-level interactions to understand further the electrochemical behavior of Pd/CeO_x-based catalysts in AEMFCs. Further improvements such as the automatic selection of local threshold values and optimizing the code to work with more than two components at the same time can help extend the usability of the developed script. Furthermore, the code can be tailored to detect and analyze other microstructural features of interest and can be optimized to be used with other formats of materials characterization data. Nevertheless, it can be asserted that the developed framework can be invaluable not only to any research focusing on improving the efficiency of Pd-CeO_x-based catalysts for AEMFCs but also to all other research endeavors aiming to contribute to the field of clean energy applications and broader.

Acknowledgments

We thank researchers at Automotive Fuel Cell Cooperation (AFCC) for the original conceptualization of the code. We are immensely grateful to the U.S. Fulbright Foreign Scholarship Program and National Science Foundation (NSF) CAREER award #2046060 for providing the opportunity and funding to carry out this research work. D.R.D.'s contribution to this study was funded by the Nancy & Stephen Grand Technion Energy Program (GTEP).

Additional Information

The authors are open to sharing of the code used in this study to promote transparency and scientific reproducibility. Please contact the corresponding author for more information.

ORCID

Mariah Batool https://orcid.org/0000-0001-8267-9560 Dario R. Dekel https://orcid.org/0000-0002-8610-0808 Jasna Jankovic https://orcid.org/0000-0001-8267-9560

References

 M. Duval, C. Moreaud, D. Couprie, Jeulin, H. Talbot, and J. Angulo, 2014 IEEE Int. Conf. Image Process. ICIP, 2014, 4862 (2014).

- D. Xia, S. Song, L. Tao, Z. Qin, Z. Wu, and Z. Gao, J. Mater. Sci. Technol., 53, 146 (2020).
- Y. Hou, Q. Li, C. Zhang, G. Lu, Z. Ye, Y. Chen, L. Wang, and D. Cao, *Engineering*, 7, 845 (2021).
- S. M. Bae, H. Y. Jung, J. H. Lee, and J. H. Hwang, J. Korean Ceram. Soc., 47, 86 (2010).
- J. Jankovic, S. Zhang, A. Putz, M. S. Saha, and D. Susac, *J. Mater. Res.*, 34, 579 (2019)
- M. Sabharwal, A. M. V. Putz, D. Susac, J. Jankovic, and M. Secanell, *ECS Trans.*, 77, 1337 (2017).
- M. Sabharwal, L. M. Pant, A. Putz, D. Susac, J. Jankovic, and M. Secanell, Fuel Cells, 16, 734 (2016).
- T. Julliand, V. Nozick, and H. Talbot, "Image Noise and Digital Image Forensics." *Digital-Forensics and Watermarking*, ed. Y.-Q. Shi et al. (Berlin)(Springer) Vol. 9569, p. 3 (2016).
- J. Jung, J. Na, H. K. Park, J. M. Park, G. Kim, S. Lee, and H. S. Kim, NPJ Comput. Mater., 7, 96 (2021).
- A. Vyas, S. Yu, and J. Paik, Multiscale Transforms with Application to Image Processing (Berlin)(Springer)p. 3 (2018).
- 11. K. Iqbal, M. Odetayo, A. James, R. A. Salam, and A. Z. H. Talib, 2010 IEEE International Conference on Systems, Man and Cybernetics, 1, 1703 (2010).
- A. Campbell, P. Murray, E. Yakushina, S. Marshall, and W. Ion, *Mater. Des.*, 141, 395 (2018).
- A. Kumar Boyat and B. Kumar Joshi, Signal Image Process. An Int. J., 6, 63 (2015).
- P. Patidar, M. Gupta, S. Srivastava, and A. K. Nagawat, Int. J. Comput. Appl., 9, 45 (2010).
- 15. S. R. Biswal, T. Sahoo, and S. Sahoo, Mater. Today Proc., 41, 357 (2021).
- M. R. Soosai, Y. C. Joshya, R. S. Kumar, I. G. Moorthy, S. Karthikumar, N. T. L. Chi, and A. Pugazhendhi, Sci. Total Environ., 780, 146469 (2021).
- 17. Z. Chen, X. Wu, and J. Vis, *Commun. Image Represent.*, **62**, 410 (2019).
- W. Cai, X. Wen, S. Wang, L. Wang, and J. Vis, Commun. Image Represent., 60, 295 (2019).
- 19. S. Salamanca, P. Merchán, A. Adán, and E. Pérez, Renew. Energy., 134, 64 (2019).
- 20. H. S. Shin, O. J. Kwon, and B. S. Oh, *Int. J. Hydrogen Energy*, 43, 20921 (2018).
- R. T. White, A. Wu, M. Najm, F. P. Orfino, M. Dutta, and E. Kjeang, *J. Power Sources*, 350, 94 (2017).
- M. J. Eslamibidgoli, F. P. Tipp, J. Jitsev, J. Jankovic, M. H. Eikerling, and K. Malek, RSC Adv., 11, 32126 (2021).
- J. Zhang, D. Kramer, R. Shimoi, Y. Ono, E. Lehmann, A. Wokaun, K. Shinohara, and G. G. Scherer, *Electrochim. Acta*, 51, 2715 (2006).
- 24. R. Roshandel and B. Farhanieh, Int. J. Hydrogen Energy, 32, 4424 (2007).
- D. S. Hwang, C. H. Park, S. C. Yi, and Y. M. Lee, *Int. J. Hydrogen Energy*, 36, 9876 (2011).
- F. C. Cetinbas, S. G. Advani, and A. K. Prasad, J. Electrochem. Soc., 160, F750 (2013).
- N. Kumano, K. Kudo, A. Suda, Y. Akimoto, M. Ishii, and H. Nakamura, J. Power Sources, 419, 219 (2019).
- 28. H. Ren, X. Meng, Y. Lin, and Z. Shao, J. Power Sources, 517, 230698 (2022).
- 29. C. Lafforgue, M. Chatenet, L. Dubau, and D. R. Dekel, ACS Catal., 8, 1278 (2018).
- 30. M. Chatenet et al., Chem. Soc. Rev., 51, 4583 (2022).
- 31. W. Zhu et al., Appl. Catal. B Environ., 299, 120656 (2021).
- H. Uchida, J. M. Song, S. Suzuki, E. Nakazawa, N. Baba, and M. Watanabe, J. Phys. Chem. B, 110, 13319 (2006).
- Y. Yu, K. F. Ludwig, J. C. Woicik, S. Gopalan, U. B. Pal, T. C. Kaspar, and S. N. Basu, ACS Appl. Mater. Interfaces, 8, 26704 (2016).
- T. Wejrzanowski, S. Haj Ibrahim, K. Cwieka, M. Loeffler, J. Milewski, E. Zschech, and C. G. Lee, J. Power Sources, 373, 85 (2018).
- A. Colliard-Granero, M. Batool, J. Jankovic, J. Jitsev, M. H. Eikerling, K. Malek, and M. J. Eslamibidgoli, *Nanoscale.*, 14, 10 (2022).
- R. T. White, D. Ramani, S. Eberhardt, M. Najm, F. P. Orfino, M. Dutta, and E. Kjeang, J. Electrochem. Soc., 166, F914 (2019).
- Y. Chen, H. Peng, D. S. Hussey, D. L. Jacobson, D. T. Tran, T. Abdel-baset, and M. Biernacki, J. Power Sources, 170, 376 (2007).
- 38. X. Liu, N. Xie, J. Xue, M. Li, C. Zheng, J. Zhang, Y. Qin, Y. Yin, D. R. Dekel, and M. D. Guiver, *Nat. Energy*, **7**, 329 (2022).
- H. A. Miller, M. Bellini, D. R. Dekel, and F. Vizza, *Electrochem. Commun.*, 135, 107219 (2022).
- D. Pinsky, N. Ralbag, R. K. Singh, M. Mann-Lahav, G. E. Shter, D. R. Dekel, G. S. Grader, and D. Avnir, *Nanoscale Adv.*, 3, 4597 (2021).
- 41. E. R. Hamo et al., ACS Catal., 11, 932 (2021).
- 42. M. Klingele, R. Zengerle, and S. Thiele, *J. Power Sources*, **275**, 852 (2015).
- F. C. Cetinbas, R. K. Ahluwalia, N. Kariuki, V. De Andrade, D. Fongalland, L. Smith, J. Sharman, P. Ferreira, S. Rasouli, and D. J. Myers, *J. Power Sources*, 344, 62 (2017).
- H. Muto, A. Shimada, T. Kaneko, N. Erdman, and C. Nielsen, *Proceedings of the Microscopy & Microanalysis 2013 Meeting*, Indianapolis, IN, USA4-8 August 2013 (Indianapolis, IN, USA)p. 53 (2013).
- 45. R. Anderhalt and L. Swenson, Micros. Today., 14, 22 (2006).
- 46. C. Lang and M. Hiscock, *Microsc. Microanal.*, **22**, 122 (2016).
- 47. M. Scimeca, S. Bischetti, and E. Bonanno, Lett. Heal. Biol. Sci., 1, 1 (2016).
- 48. B. R. Jany, A. Janas, and F. Krok, *Micron*, 130, 102800 (2020).
- V. D. Hodoroaba, S. Rades, T. Salge, J. Mielke, E. Ortel, and R. Schmidt, IOP Conf. Ser.: Mater. Sci. Eng., 109, 1 (2016).
- P. T. Durdziński, C. F. Dunant, M. Ben Haha, and K. L. Scrivener, *Cem. Concr. Res.*, 73, 111 (2015).

- 51. H. Hao, R. Guo, Q. Gu, and X. Hu, Miner. Eng., 143, 105899 (2019).
- 52. C. Li, D. Wang, and L. Kong, J. Pet. Sci. Eng., 200, 108178 (2021).
- A. Tilson and M. Strauss, 2018 IEEE International Symposium on the Physical and Failure Analysis of Integrated Circuits (IPFA) (IEEE) Vol. 1, p. 1 (2018).
- Z. Zhong, J. Roller, O. Bidiuk, J. Blackwood, M. Verheijen, O. Ugurlu, and J. Donald, *Microsc. Microanal.*, 23, 1458 (2017).
- 55. P. Macioł, J. Falkus, P. Indyka, and B. Dubiel, *Materials*, 14, 4507 (2021).
- J. T. Held, K. I. Hunter, N. Dahod, B. Greenberg, D. Reifsnyder Hickey, W. A. Tisdale, U. Kortshagen, and K. A. Mkhoyan, ACS Appl. Nano Mater., 1, 989 (2018).
- 57. N. Macauley et al., Adv. Energy Mater., 12, 2201063 (2022).
- C. Lei, F. Yang, N. Macauley, M. Spinetta, G. Purdy, J. Jankovic, D. A. Cullen, K. L. More, Y. S. Kim, and H. Xu, J. Electrochem. Soc., 168, 044517 (2021).
- C. Wang, M. Ricketts, A. P. Soleymani, J. Jankovic, J. Waldecker, and J. Chen, J. Electrochem. Soc., 168, 044507 (2021).
- C. Wang, M. Ricketts, A. P. Soleymani, J. Jankovic, J. Waldecker, J. Chen, and C. Xu, J. Electrochem. Soc., 168, 034503 (2021).
- E. B. Tetteh, H. Y. Lee, C. H. Shin, S. H. Kim, H. C. Ham, T. N. Tran, J. H. Jang, S. J. Yoo, and J. S. Yu, ACS Energy Lett., 5, 1601 (2020).
- 62. J. Mo et al., Int. J. Hydrogen Energy, 42, 27343 (2017).
- E. Park, S. Taniguchi, T. Daio, J. T. Chou, and K. Sasaki, *Int. J. Hydrogen Energy*, 39, 1463 (2014).
- 64. D. R. Dekel, J. Power Sources, 375, 158 (2018).
- S. Gottesfeld, D. R. Dekel, M. Page, C. Bae, Y. Yan, P. Zelenay, and Y. S. Kim, J. Power Sources, 375, 170 (2018).
- J. C. Douglin, J. R. Varcoe, and D. R. Dekel, J. Power Sources Adv., 5, 100023 (2020).
- C. G. Arges, V. Ramani, and P. N. Pintauro, *Electrochem. Soc. Interface*, 19, 31 (2010).
- T. J. Omasta, X. Peng, H. A. Miller, F. Vizza, L. Wang, J. R. Varcoe, D. R. Dekel, and W. E. Mustain, J. Electrochem. Soc., 165, 13039 (2018).
- N. Ralbag, E. S. Davydova, M. Mann-Lahav, P. Cong, J. He, A. M. Beale, G. S. Grader, D. Avnir, and D. R. Dekel, J. Electrochem. Soc., 167, 054514 (2020).
- J. Zhang, W. Zhu, T. Huang, C. Zheng, Y. Pei, G. Shen, Z. Nie, D. Xiao, Y. Yin, and M. D. Guiver, Adv. Sci., 2100284, 1 (2021).

- Y. Cao, R. Ran, X. Wu, B. Zhao, J. Wan, and D. Weng, *Appl. Catal. A Gen.*, 457, 52 (2013).
- T. Kolli, K. Rahkamaa-Tolonen, U. Lassi, A. Savimäki, and R. L. Keiski, Catal. Today, 100, 297 (2005).
- 73. S. Sahoo, D. R. Dekel, R. Maric, and S. P. Alpay, ACS Catal., 11, 2561 (2021).
- 74. S. Lu and Z. Zhuang, J. Am. Chem. Soc., 139, 5156 (2017).
- 75. R. K. Singh et al., Adv. Funct. Mater., 30, 2002087 (2020).
- 76. S. Darija et al., ECS Meet. Abstr, MA2016-02, 2593 (2016).
- 77. C. Fischer and I. Kakoulli, Stud. Conserv., 51, 3 (2006).
- 78. J. Bentley, J. E. Wittig, and J. R. McBride, Microsc. Microanal., 20, 610 (2014).
- C.-I. Chang, Hyperspectral Imaging: Techniques for Spectral Detection and Classification (Berlin)(Springer)p. 15 (2003).
- 80. P. Horny, L. Eric, C. Helen, and G. Raynald, Microsc. Microanal., 16, 821 (2010).
- 81. Y. Zhang and X. Shi, Adv. Mater. Res., 940, 433 (2014).
- 82. C. A. McMahon and D. J. Pitt, Mater. Des., 16, 3 (1995).
- 83. F. D. Speck et al., Chem. Mater., 32, 7716 (2020).
- H. Yu, E. S. Davydova, U. Ash, H. A. Miller, L. Bonville, D. R. Dekel, and R. Maric, *Nano Energy.*, 57, 820 (2019).
- J. Ahn, M. I. Ali, J. H. Lim, Y. Park, I. K. Park, D. Duchesne, L. Chen, J. Kim, and C. H. Lee, *Membranes*, 11, 143 (2021).
- J. Zhang, W. Zhu, T. Huang, C. Zheng, Y. Pei, G. Shen, Z. Nie, D. Xiao, Y. Yin, and M. D. Guiver, Adv. Sci., 8, 2100284 (2021).
- J. Qi, N. Benipal, H. Wang, D. J. Chadderdon, Y. Jiang, W. Wei, Y. H. Hu, and W. Li. *Chem. Sus Chem.* 8, 1147 (2015).
- 88. S. Kamarajugadda and S. Mazumder, J. Power Sources, 183, 629 (2008).
- E. N. Codaro, R. Z. Nakazato, A. L. Horovistiz, L. M. F. Ribeiro, R. B. Ribeiro, and L. R. O. Hein, *Mater. Sci. Eng. A*, 334, 298 (2002).
- A. Bescond, J. Yon, F. X. Ouf, D. Ferry, D. Delhaye, D. Gaffié, A. Coppalle, and C. Rozé, Aerosol Sci. Technol., 48, 831 (2014).
- I. S. Bessa, V. T. F. Castelo Branco, and J. B. Soares, *Constr. Build. Mater.*, 37, 370 (2012).
- A. Scozzafava, L. Tomesani, and A. Zucchelli, J. Mater. Process. Technol., 153–154, 853 (2004).
- 93. A. Sochan, P. Zieliński, and A. Bieganowski, Sediment. Geol., 327, 14 (2015).
- 94. C. Liu, B. Shi, J. Zhou, and C. Tang, *Appl. Clay Sci.*, **54**, 97 (2011).